Title:

Kinematic rupture model of the February 6th 2023 Mw7.8 Turkey earthquake from a large set of near-source strong motion records combined with GNSS offsets reveals intermittent supershear rupture

Authors:

Bertrand DELOUIS (corresponding author) delouis@geoazur.unice.fr

Université Côte d'Azur, CNRS, IRD, Observatoire de la Côte d'Azur, Géoazur, 250 rue Albert Einstein, 06560 Valbonne, France

Martijn VAN DEN ENDE Martijn.VANDENENDE@oca.eu

Université Côte d'Azur, CNRS, IRD, Observatoire de la Côte d'Azur, Géoazur

Jean-Paul AMPUERO ampuero@geoazur.unice.fr

Université Côte d'Azur, IRD, CNRS, Observatoire de la Côte d'Azur, Géoazur

The authors acknowledge there are no conflicts of interest recorded

Key points

1. **We infer the kinematic slip history of the 2023 M7.8 Turkey earthquake from unprecedentedly-dense near-fault strong motion data**

2. **We identify several portions of the East Anatolian Fault where the rupture is transiently supershear**

3. **We associate transitions to supershear speed with regions of reduced fault slip, which could relate to failure of local rupture barriers**

Abstract

The 2023 M7.8 SE Turkey earthquake was recorded by an unprecedentedly large set of strong motion stations very close to its rupture, opening the opportunity to observe the rupture process of a large earthquake with fine resolution. Here, the kinematics of the earthquake source is inferred by finite source inversion based on strong motion records and coseismic offsets from permanent GNSS stations. The strong motion records at stations NAR and 4615, which are closest to the splay fault where the rupture initiated and which were previously interpreted as containing the signature of supershear rupture speeds, are successfully modeled here by a sub-shear rupture propagating unilaterally to the NE. Once the rupture on the splay fault reaches the East Anatolian Fault (EAF), it propagates on the EAF bilaterally, extending about 120 km NE and 180 km SW. To

the South, the depth extent of the rupture decreases as it passes a bend of the EAF. While the rupture velocity remains globally sub-shear along the EAF, we identify several portions of the fault where the rupture is transiently supershear. The transitions to supershear speed coincide with regions of reduced fault slip, which suggests supershear bursts generated by failure of local rupture barriers. Towards the SW termination, the rupture encircles an asperity before its failure, which is a feature that has been observed only on rare occasions. This unprecedented detail of the inversion was facilitated by the proximity to the fault and the exceptional density of the accelerometric network in the area.

Introduction

The February 6, 2023 (01H17 UTC) earthquake of moment magnitude (Mw) 7.8 in SE Turkey (Pazarcık, Kahramanmaraş, Türkiye) involved three major fault segments well differentiated by location and orientation (e.g. Melgar et al., 2023). The rupture started on a fault branch that splays off from the East Anatolian Fault (EAF) and runs adjacent to the city of Narli where strong motion stations 4615 and NAR are located **(Figure 1**). This splay fault is sometimes referred to as the Narli Fault, however Melgar et al. (2023) referred to it as the Nurdağı-Pazarcık Fault; it will be called hereafter the splay fault (SPF). The rupture later propagated on two segments of the EAF.

In principle the time-dependent earthquake rupture process can be constrained by seismological data, but in practice such efforts are often limited by the scarcity of near-source recordings. Our objective here is to take advantage of the existence of numerous strong motion stations in the immediate vicinity of the ruptured fault segments to determine with fine resolution the characteristics of the rupture in space and time. GNSS static coseismic offsets are also used to

59 further constrain the spatial distribution of slip. Previous studies (USGS 2023; Melgar et al. 2023)
60 have highlighted the general characteristics of the earthquake by combining different types of
61 data, but using only a limited number of strong motion stations (< 15). So far, the potential for
62 source inversion enabled by the dense strong motion network installed in the area by the Turkish
63 Disaster and Emergency Management Authority (AFAD) has only been partially exploited. In
64 particular, the signals from two stations very close to the splay fault (NAR and 4615) were
65 proposed to contain evidence for supershear rupture on this branch of the rupture (Rosakis et al.,
66 2023), but these signals have not yet been modeled by source inversion studies. Moreover, earlier
67 studies of this earthquake reported sub-shear speeds on the EAF. Here, exploiting the complete
68 dataset we gain further insights into the evolution of rupture speed during this earthquake.

69 In this study we model a large set of 31 strong motion stations, including the closest ones to the
70 rupture segments, plus the available horizontal coseismic offsets from 20 GNSS stations. These
71 data are inverted jointly to constrain the parameters of a kinematic source model of the Mw 7.8
72 earthquake. Our inversion results provide a view of the rupture process, including the spatial
73 variability of rupture speed, with an unprecedented level of resolution.

74

75 **Strong motion data**

76 A very dense set of near-field strong motion records (3 components: NS, EW and vertical) from
77 the Turkish National Strong Motion Network have been made publicly available by the Disaster
78 and Emergency Management Authority (AFAD) through the Turkish Accelometric Database and
79 Analysis System (TADAS). We selected 31 stations covering the entire rupture zone, including

stations located very close to the ruptured segments (**Figure 1**). Signal processing includes removal of the pre-event mean amplitude, double integration to displacement, and bandpass filtering. The low frequency cutoff varies between 0.005 and 0.06 Hz, depending on the amount of long-period noise observed after the double integration. The high-frequency cutoff is set to 0.3 Hz, corresponding to the highest frequency at which we judge waveforms can be modeled adequately using a simple velocity model for wave propagation. Synthetic seismograms are computed by the wavenumber integration method of Bouchon (1981) adopting a 1D velocity model (**Table S1** in the electronic supplement to this article) derived from the regional velocity model determined by Güvercin et al. (2022). On the fault segment located in the immediate vicinity of the NAR and 4615 stations (segment 1bis, see model description in Section “Kinematic model, inversion method, and constraints on rupture parameters''), we computed synthetic waveforms using exact expressions for the displacement field at the surface of a uniform elastic half-space (Johnson, 1974), including near-field waves, as implemented in Legrand (1995).

GNSS data

Coseismic static offsets obtained from GNSS time series were made available by the Nevada Geodetic Laboratory for stations from the CORS (Continuous Operating Reference Stations) network, calculated with final orbits from the NASA Jet Propulsion Laboratory (JPL) on 26 February 2023. We selected the horizontal offsets at 20 stations closest to the rupture zone (**Figure 1**). We calculated synthetic static displacements using the formulation of Savage (1981) for dislocations in an elastic half-space

Kinematic model, inversion method, and constraints on rupture parameters

We define the kinematic model and conduct the finite source inversion following a similar approach to that used by Delouis et al. (2002) to model the 1999 Izmit (Mw 7.6) earthquake. The rupture is represented by rectangular fault segments, subdivided into small dislocation surfaces (subfaults) to model static surface displacements, and represented by a point source at their center to model seismic waveforms. The model and subfault dimensions are provided in **Table 1** and their surface projection is shown in **Figure 1**.

The local source time function associated with each point source is represented as the sum of three isosceles triangular moment rate functions, mutually overlapping, each with a total duration of 4 s. Two bounding rupture velocities, called Vrmin and Vrmax, limit the rupture onset times along the fault by enforcing the constraint $V_{rmin} \leq dist_{subfault} / onset_{time} \leq V_{rmax}$. Here we define dist_subfault as the distance along the fault segments between the subfault center and the rupture initiation point. The latter is set as the hypocenter for segments 1 and 1bis which represent the splay fault (SPF), and as the junction between SPF and EAF for segments 2 and 3 which represent the EAF itself **(Figure 1**). This constraint has the following physical meaning: at any given location along the faults, the average rupture slowness (defined as the rupture slowness spatially averaged over horizontal along-fault distance between the rupture initiation point and the given location) is constrained to lie between 1/Vrmax and 1/Vrmin. Within the constrained range, the rupture onset times are allowed to vary freely, thus the rupture speeds at any point of the fault (called hereafter the local rupture speed) can lie beyond the Vrmin - Vrmax range (see **Figure S1** for an illustration, in the electronic supplement to this article).

The inverted parameters are, for each subfault, the rupture onset time, the amplitudes of the triangular functions, and the rake angle. The inversion itself is carried out with a simulated annealing algorithm. The cost function to be minimized is a weighted sum of the normalized RMS (root mean square) misfit functions for each dataset, plus a seismic moment minimization function and a smoothing function.

The strong motion stations are located much closer to the rupture than the GNSS stations (**Figure 1a**), thus they are more sensitive to fine details of the rupture and more difficult to model. Consequently, a lower weight (w=0.4) is assigned to the GNSS data than to the strong motion data (w=1.0). The weights assigned to the seismic moment minimization and smoothing functions are adjusted so as not to incorporate excess seismic moment for little gain in data fit, and to avoid incorporating a level of detail in the model that is poorly constrained by the data.

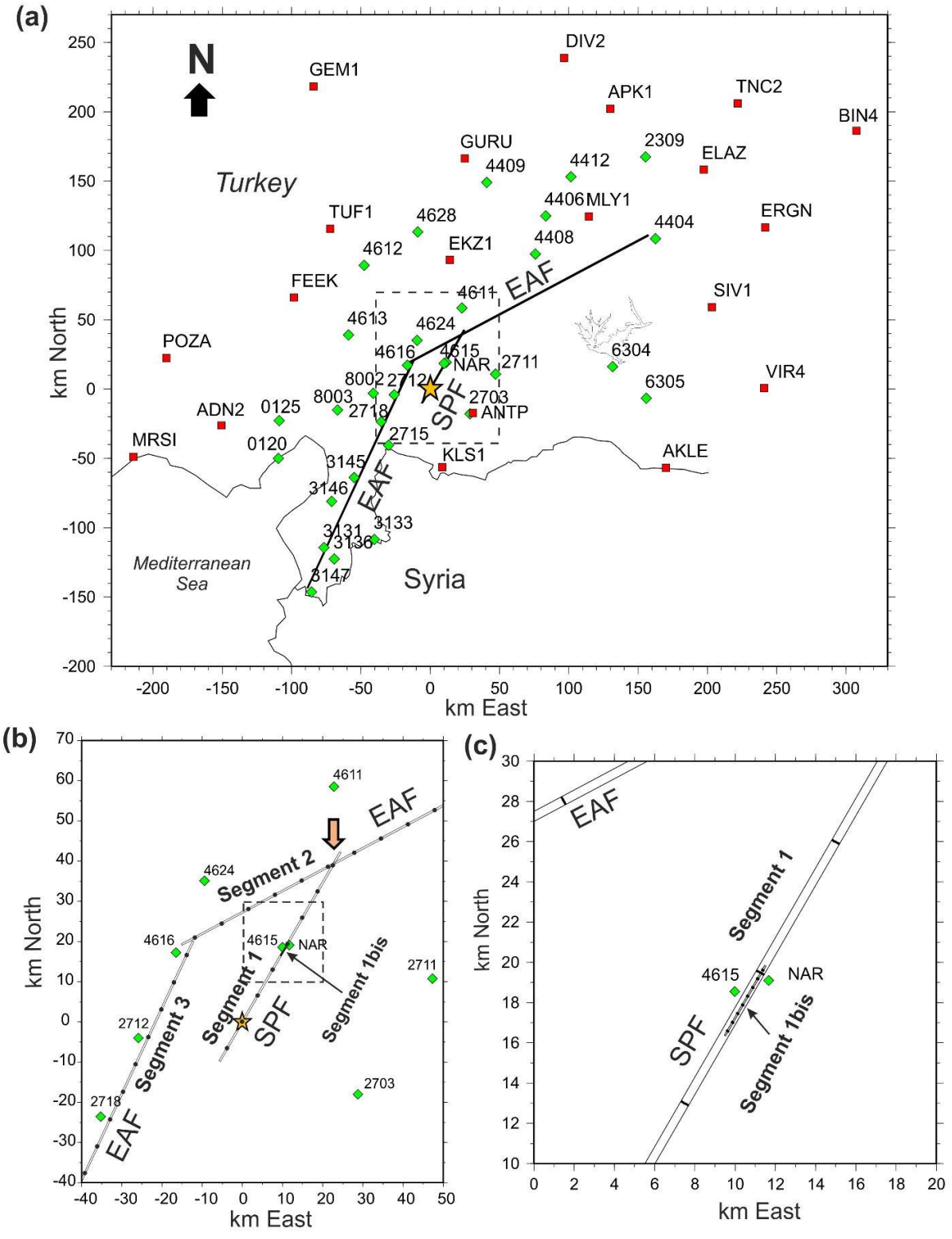
(a)
N
Turkey
Syria
Mediterranean Sea
EAF
SPF
DIV2
GEM1
APK1
TNC2
BIN4
GURU
2309
ELAZ
4409
4412
4406
MLY1
ERGN
TUF1
4628
4404
4612
EKZ1
4408
FEEK
4611
SIV1
4613
4624
POZA
4616
4615
NAR
2711
6304
8002
2712
VIR4
6305
8003
2718
2703
ADN2
0125
ANTP
2715
MRSI
0120
KLS1
AKLE
3145
3146
3133
3131
3136
3147
km North
km East
(b)
4611
EAF
4624
Segment 2
4616
4615
NAR
Segment 1bis
2711
Segment 1
Segment 3
2712
SPF
2703
2718
EAF
km North
km East
(c)
EAF
Segment 1
4615
NAR
SPF
Segment 1bis
km North
km East

133

Figure 1. (a) Overview map showing the strong motion (green diamond) and GNSS (red squares) stations used in this study, with corresponding names. Thick black line: surface trace of the fault model. Orange star: epicenter of the mainshock (37.22°N, 37.025°E, this study) at the origin of the coordinates (0,0). The dashed box indicates the zone (b). **(b)** Close-up of the epicentral area. Thin lines with small dots show the fault model with the position of the point sources (simplified representation, each dot corresponding in reality to 5 points distributed along dip), projected on the earth surface. The names of the fault segments are shown. The dashed frame indicates the zone (c). Orange arrow: junction between segment 1-1bis (splay fault) and segment 2 (East Anatolian Fault). **(c)** Close-up of the area where the fault model passes between the strong motion stations 4615 and NAR and where a finely discretized fault segment 1bis is used. SPF: splay fault; EAF: East Anatolian Fault.

The hypocenter has been located by many agencies, systematically more than 15-20 km south of the EAF (e.g. AFAD, KOERI, USGS). As in Melgar et al. (2023), we consider that the hypocenter occurred on a NNE-SSW fault branch, a splay fault (SPF, **Figure 1**) with respect to the EAF. Using P arrival times and a few S arrival times at the nearby strong motion stations, we located the epicenter of the main shock at 37.22°N and 37.025°E, with an estimated uncertainty of less than 5 km, using the GRIDSIMLoc nonlinear approach (Delouis et al., 2022). However, the hypocenter depth, ranging from 3 to 20 km, is not well constrained by the arrival times. We used this epicenter to define the rupture initiation point in our kinematic slip model, and tested different

hypocenter depths based on the discretization of our rupture model. Finally, the best results were obtained with a hypocenter depth of 12.5 km, but the inversion results are not very sensitive to variations of this parameter within +/- 5 km.

The rupture model includes three fault segments, corresponding to the minimum degree of complexity to represent to first order the rupture geometry constrained by satellite imagery, aftershock distribution and field observations (e.g. map from the USGS Turkey Earthquake Emergency Response (Reitmann et al., 2023), and the compilation of documentation on the Kahramanmaraş Supersite science web page, see Data and resources). Segment 1 corresponds to the NNE-SSW trending splay fault hosting the hypocenter. Segments 2 and 3 correspond to the NE-SW segment (striking N62) and NNE-SSW segment (striking N25) of the EAF, respectively (**Figure 1** and **Table 1**). On all segments, we allow the rake to vary by +/- 45° around the central value of 0 corresponding to a dominant left-lateral strike-slip motion (**Table 1**). In initial inversions, we allowed the dip of fault segments to vary between 80 and 90 degrees, to the NW or SE, but we observed no real impact on the data modeling. Since the data do not appear to be very sensitive to the choice of dip when it is close to vertical, we set it at 89° to the SE for all segments.

Preliminary constraints on rupture speeds

Two accelerometer stations were the focus of special attention, as their positioning is of primary importance to constrain the initial phase of the rupture on the SPF. These are stations 4615 and NAR, the closest ones to the epicenter. Between these two stations, separated by only 1.8 km,

177 surface breaks have been identified, with displacements of the order of 2.6 to 2.8 m (**Figure S2** in
178 the electronic supplement to this article). This is strong evidence that these stations are located
179 on opposite sides of the ruptured splay fault. Coseismic surface offset along this same fault
180 segment have been also evidenced by the analysis of SAR (synthetic Aperture Radar) images and
181 direct field observations (e.g. Karabulyt et al., 2023; Karabacak et al., 2023).

182 A major pulse, clearly visible on the velocity seismograms and marked by a maximum
183 displacement of 210 cm southward at station 4615 and 90 cm northward at station NAR, starts
184 about 4.8 s after the first arrival of the P-wave at these two stations (**Figure S3** in the electronic
185 supplement to this article). We interpret this part of the signal as being produced by the left-
186 lateral surface faulting between the two stations. The rupture, located less than one kilometer
187 from the stations, moves 4615 southward and NAR northward. The reversal of the direction of
188 displacement and the magnitude of the displacement observed at these two stations so close to
189 each other appears to be the direct signature of a local fault offset of at least 3 m (2.1 + 0.9 m),
190 in agreement with the surface observations (**Figure S2** in the electronic supplement to this
191 article).

192 Modeling the first 15 seconds of the signal following the P-wave onset at stations 4615 and NAR
193 required special effort. We found it necessary to incorporate a finely discretized portion of the
194 fault between the two stations, denoted as segment 1bis (**Table 1** and **Figure 1b-c**). The synthetic
195 seismograms generated by segment 1bis for stations 4615 and NAR were calculated using the
196 exact analytical solution for a homogeneous half-space of Johnson (1974), which is more accurate
197 for very small source-station distances than the numerical approach by wavenumber integration

198 (Bouchon 1981). The homogeneous velocity model assumed has P-wave velocity of 4.90 km/s and
199 S-wave velocity of 2.83 km/s.

200 Rosakis et al. (2023) made observations suggesting that a transition from subshear to supershear
201 rupture velocity (Vr) occurred on SPF between stations 4615 and NAR. To examine the rupture
202 velocity on the splay fault, we performed a series of inversions where Vr on segments 1 and 1bis
203 is fixed to a constant value varying from 2.0 to 5.0 km/s. **Figure 2a** shows the variation of RMS fit
204 of all 31 stations on the one hand, and of the two stations 4615 and NAR on the other hand, as a
205 function of the fixed Vr value. The effect of the choice of Vr on the modeling of the north
206 component of 4615 and NAR is illustrated in **Figure 2b**. Best results are obtained for constant Vr
207 in the range 2.8 to 3.0 km/s, with already good results for Vr=2.5 km/s. This indicates that, to
208 model displacement waveforms in the frequency band used here, it is not necessary for Vr to
209 transition from sub-shear to supershear. We will come back to this point in the discussion. In our
210 final inversion, we relax the constraint of a constant Vr on the splay fault by allowing the average
211 Vr to vary between Vrmin = 2.5 km/s and Vrmax = 3.3 km/s.

212

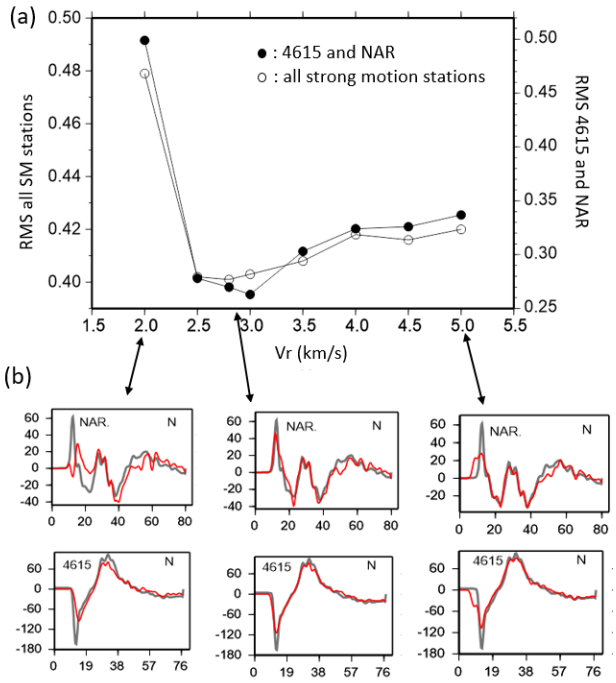

Figure 2. Exploration of the rupture velocity (Vr) on segments 1 and 1bis. **(a)** RMS waveform misfit value for all strong motion stations (SM) and for 4615 and NAR only as a function of fixed constant Vr values. **(b)** North component waveform fit for NAR and 4615 stations for constant Vr values of 2.0, 2.8 and 5.0 km/s. Waveforms are in displacement and bandpass filtered between 0.01 and 0.3 Hz. Only the north components of NAR and 4615, being the most sensitive to Vr and the most difficult to model, are shown but the inversion is performed with the three components N, E and Z of all strong motion stations.

225 During initial inversions, we observed that slip on segments 1 and 1bis (SPF) could reach 6 m, in
226 disagreement with independent evidence of surface offsets of no more than 3 m along this fault
227 section (**Figure S2** in the electronic supplement to this article). Although it cannot be ruled out
228 that slip at depth may exceed slip at the surface, we noted that the fit of the data was not
229 significantly improved when the maximum slip on these segments increased from 4 to 6 m. In the
230 final inversion the slip on segments 1 and 1bis is limited to 4 m.

231 Regarding the EAF (segments 2 and 3), optimum results are obtained by using Vrmin = 2.0 km/s
232 and Vrmax = 4.0 km/s. Expanding the range Vrmin - Vrmax beyond these limits does not produce
233 a significant improvement in data fit. The maximum allowed slip on the EAF was explored
234 between 5 and 12 m. The improvement in the fit of the data becomes small for a maximum slip
235 greater than 7 to 8 m, and slip was limited to 8 m in the final inversion. However, the maximum
236 slip on the EAF is not constrained with an uncertainty better than +/- 1 to 2 m.

237

Segment	Strike (°)	Dip (°)	Central rake (°)	L (km)	W (km)	Δl (km)	Δw (km)	Vrmin (km/s)	Vrmax (km/s)
1	30	89	0	60	25	7.5	5.0	2.5	3.3
1bis	30	89	0	4	5	0.5	1	2.5	3.3
2	62	89	0	195	25	7.5	5.0	2.0	4.0
3	25	89	0	180	25	7.5	5.0	2.0	4.0

238

239 **Table1.** Fixed parameters for the fault segments of the kinematic rupture model. L:
240 length; W: width; Δl and Δw subfault length and width. Vrmin and Vrmax: bounding
241 rupture velocities. The top of all segments is located at the free surface.

242 A lower bound is imposed on the initiation time of rupture on the main EAF fault for two reasons.
243 1) to avoid a rupture that is too strongly non-causal, and 2) to define the time after which the

reference point used to compute distances for rupture velocity is no longer the hypocenter but the junction between the splay fault (SPF) and the EAF. This lower bound enforces a delay of the EAF rupture initiation relative to the hypocentral time, but allows for uninterrupted rupture across the junction

In relation to point 1), if no delay to rupture initiation on the EAF were imposed, the limiting value of vrmax of 4 km/s on the EAF main fault (segments 2, **Table 1**) would permit the rupture to start on the EAF well before it has finished propagating on the initial splay fault. In relation to point 2), given the very different orientation of the initial fault and the EAF, and the possibility for rupture to propagate in two different directions on the EAF (NE and SW), the junction must be redefined as a new reference initiation point for rupture at a specific time. From that time on, distances for segments 2 and 3 are calculated from the junction and along the EAF, rather than from the hypocenter. The delay is simply imposed in the inversion as the minimum rupture onset time for subfaults of segment 2 and 3.

This delay cannot be easily inverted for, but we tested different delay values (relative to the hypocenter origin time) ranging from 10 to 18 s and retained the value of 14 s which gives the best fit of the data. However, we recognize that this parameter is not defined with an accuracy better than a few seconds, and that the inversion has the possibility of delaying the slip on the EAF a little further if the data demand it. The imposition of this delay does not necessarily mean that the rupture stops before propagating on the main EAF fault. It allows for a continuous, natural progression of the rupture from the splay fault to the main fault.

Final slip model and rupture timing

We present here the final slip model resulting from the joint inversion of the strong motion and GNSS static data. The spatial distribution of slip is shown in **Figure 3**. The spatial and temporal distribution of the slip is presented on **Figures 4, 5, 6**, **and 7** separately for the SPF (segments 1 and 1bis) and for the EAF (segments 2 and 3).

On the SPF, the rupture is unilateral to the NNE. The total slip is limited at the hypocenter and south of it. Beyond about 15-20 km NE from the epicenter, slip is mainly localized near the surface, between stations 4615 and NAR, and at the end of the SPF at its junction with the EAF. From the junction on, the rupture propagates bilaterally on the EAF, for about 120 km to the NE and 180 km to the SW. On segment 2 slip reaches 20-25 km depth, whereas on segment 3 it is shallower, localized above 10 km depth. Along the whole rupture, the maximum slip is found close to the surface. It reaches our maximum allowed value of 8 m on both segments of the EAF.

On the EAF, slip at the junction with the splay fault is small, but it may be partially compensated by slip at the NNE termination of the splay fault. The slip observed at the NE end of segment 2 is likely an artifact, possibly related to a geometric complexity of the rupture not taken into account in the model.

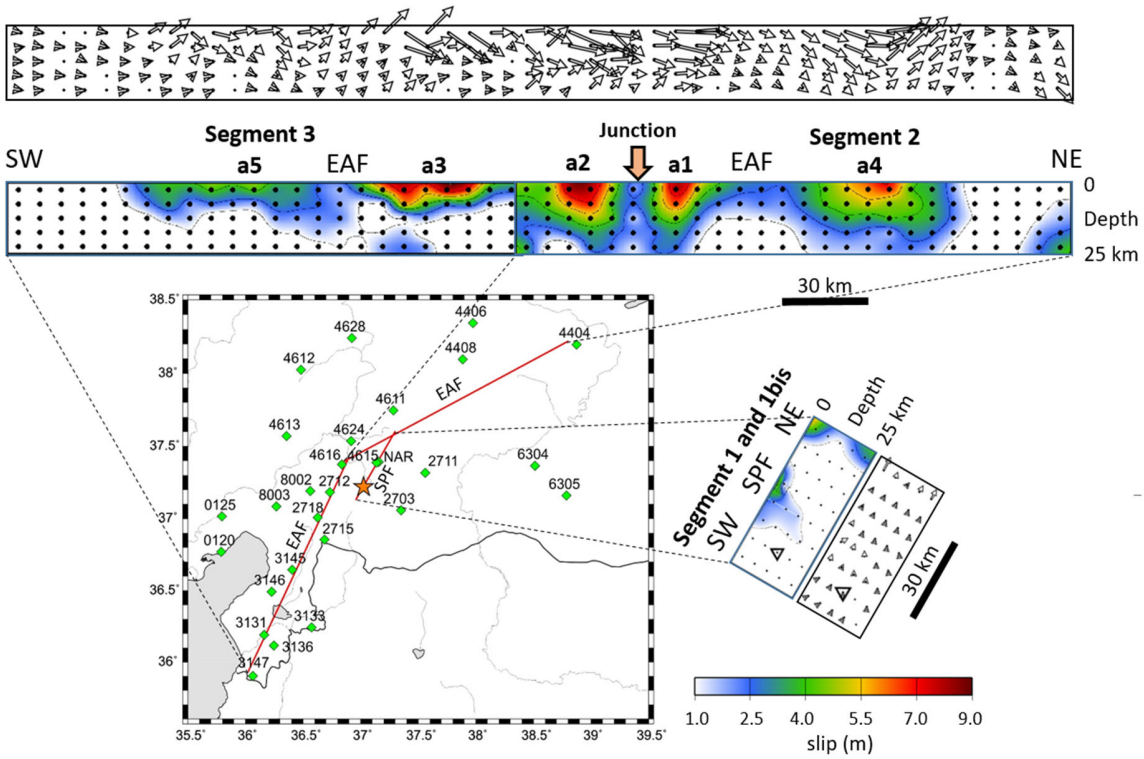

Figure 3. Slip distribution from the joint inversion of strong motion and GNSS data on the three segments of the kinematic model, and relation with the map view. SPF: splay fault; EAF East Anatolian Fault. On the map, the epicenter, the surface trace of the rupture model, and the strong motion stations are represented by the orange star, the red lines and the green diamonds respectively. The hypocenter on segment 1-1bis (SPF) is marked by the open triangle. The junction between the splay fault (SPF, segment 1) and Segment 2 of the EAF is marked by the orange arrow. a1 to a5: labels for the main slip areas along the EAF. The slip direction is indicated by the open arrows scaled with slip amplitude.

On the SPF, the rupture propagates horizontally at a near constant rupture velocity of 2.5 to 3.1 km/s (**Figure 4a**). In the time interval between 12 and 20 s, the rupture front is faint and difficult to follow on the slip velocity snapshots (**Figure 6a**) and little slip is accumulated (**Figure 6b**). After 20 s, larger slip emerges near the junction with the EAF.

Along the EAF, the average rupture velocity calculated from the junction with the splay fault remains below 3 km/s along segment 2 and close to 3 km/s over most of segment 3. (**Figure 4b**). However, we identify notable local deviations from this average trend.

To analyze the inversion results, we estimate the local rupture speed and acceleration (horizontal apparent values) by tracking the onset of slip on the sub-faults (**Figure 5**). We determine the apparent rupture acceleration, as a function of along-strike distance, that minimizes the difference between the observed position of the rupture front and the double integral of the rupture acceleration, with a mild smoothness constraint on the acceleration. The resulting acceleration is integrated once to obtain the rupture speed along the fault.

Initially and up to a distance of about 30 km from the junction, rupture propagates both to the NE and to the SW at a relatively low speed, between 2 and 2.5 km/s, generating two main slip areas we denote as a1 and a2 (**Figures 4b, 5, and 7**). Then, we observe a pattern common to both rupture directions: after running through a low slip section (gray areas on **Figure 5**), rupture speed increases when entering into the next high slip area (a3, a4, a5), reaching locally a value of 4 km/s or more, maintained over a distance of 20 to 30 km (red F markers on **Figure 5c**, and on **Figure**

313 **7a**). This pattern involves multiple transitions from sub-shear to supershear rupture speed along
314 the EAF at the scale of a few tens of kilometers.

315 As an independent verification of the rupture trajectory along Segment 3, we inspected the strong
316 motion waveforms of selected receivers closest to the fault (**Figure S4 in the electronic**
317 **supplement to this article**). The three-component waveforms were bandpass filtered from 1 to 5
318 Hz, after which we computed the amplitude of motion as $A=\sqrt{(N^2+E^2+Z^2)}$ for components N, E, and
319 Z. The passage of the rupture was clearly visible as a strong pulse in the amplitude time series,
320 the timing of which was manually picked. To acknowledge uncertainty in the onset time due to
321 the emergent onset, an onset time range was selected; this time range is indicated in **Figure 4b**,
322 and verifies the rupture trajectory inferred by source inversion. Notably, the manual picks confirm
323 the existence of brief supershear phases along Segment 3.

324 The lateral progression of the rupture generally takes place first at or near the surface (**Figures 6**
325 **and 7**). There is one notable exception: around the main slip area a5 on segment 3, the snapshots
326 at 56 s of slip velocity and cumulative slip (**Figure 7a and b**, green U mark) show that rupture
327 propagates first at 10-12 km depth, leaving unbroken the shallowest portion of the fault. This
328 shallow part slips a few seconds later (see the next snapshot at 59 s). Such a delayed rupture of
329 an asperity after it has been surrounded by slip has been described by Zhang et al. (2012) for the
330 2008 Mw 7.9 Wenchuan earthquake in China, and by Meng et al (2018) for the 2015 Mw 8.3
331 Illapel earthquake in Chile, though here it is observed at a smaller scale. Although quite a large
332 flexibility in rupture timing is allowed in our approach, we do not observe clear backpropagation,
333 i.e. slip propagating towards the hypocenter (**Figure 6a and 7a**).

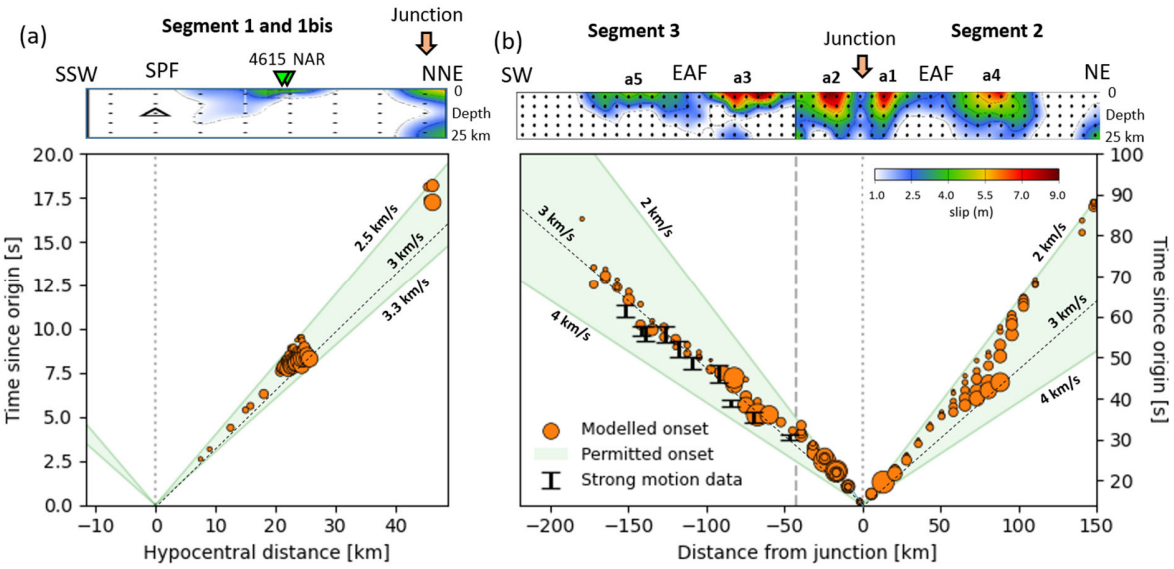

Figure 4. Time-distance plots of slip for segments 1 and 1bis **(a)** and for segments 2 and 3 **(b)** from the joint inversion of strong motion and GNSS data**.** SPF: splay fault; EAF: East Anatolian Fault; orange dots: subfault timing at a function of distance, with size proportional to slip (larger than 1 m). Green shaded area: allowed domain for average rupture speed. Oblique black line: average rupture speed 3 km/s. Lines of average rupture speed start from the hypocenter in **(a)** and from the junction between the splay fault (segment 1) and the EAF (segment 2) in **(b)**. The slip distribution along strike and dip is shown above the graphs. On top of **(a)**, the position along strike of strong motion stations 4615 and NAR is indicated, and on top of **(b)**, the junction with the splay fault is indicated by the orange arrow. a1 to a5: labels for the main slip areas along the EAF.

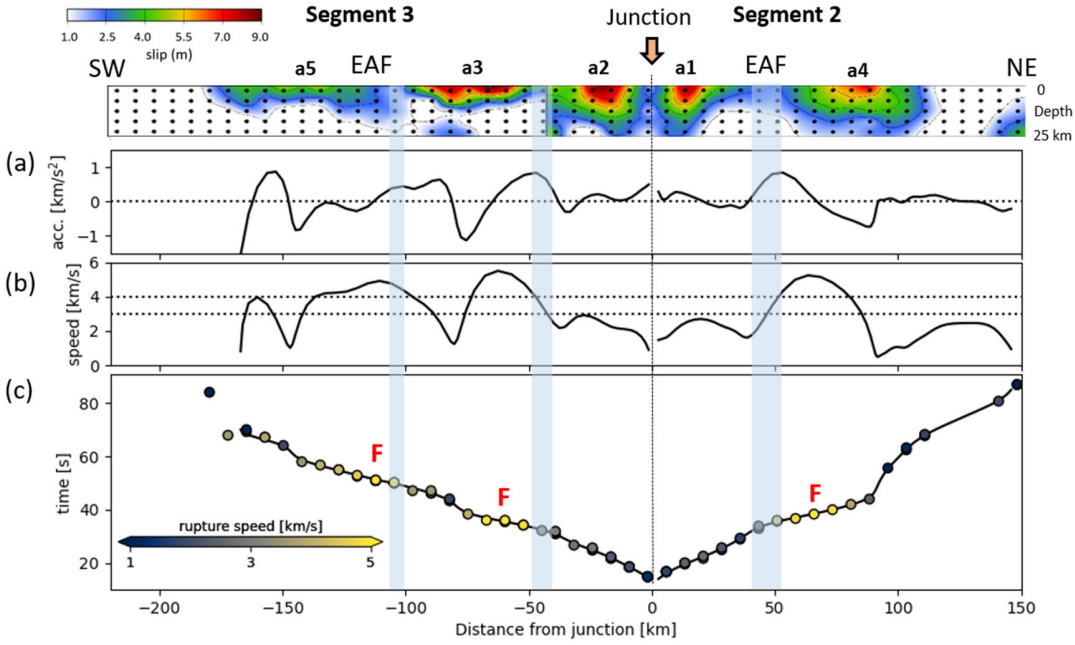

348

349 **Figure 5**. Estimation of rupture speed as a function of distance from the junction along
350 the EAF (Segment 2 and 3). **(a)** Inverted rupture acceleration. **(b)** Local rupture speed
351 (integral of acceleration). **(c)** Black curve: rupture onset time (related to the second
352 integral of acceleration). The markers represent the observed onset times colored
353 according to the estimated local rupture speed. Compared to **Figure 4b**, only the
354 subfaults whose time is less than 1 s from the rupture front at a given horizontal
355 position are included in the inversion and panel c. The shaded regions indicate the
356 locations of low slip. F (fast) markers in red point to areas of high local speed, reaching
357 supershear. Slip map on top with the same labels as in previous figures.

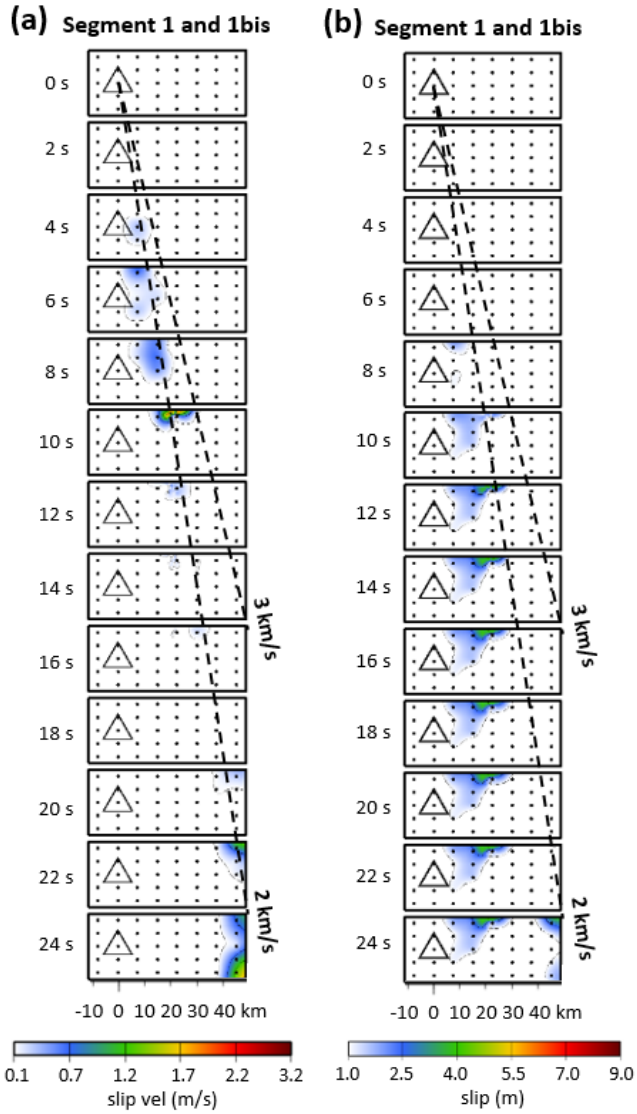

Figure 6. Snapshots of the space-time evolution of the rupture on segments 1 and 1bis (splay fault) from the joint inversion of strong motion and GNSS data. **(a)** slip velocity at each time step, **(b)** cumulative slip. Time steps are indicated on the left side. Open triangle: hypocenter. Oblique dashed black lines: reference slopes corresponding to average rupture velocities (Vr) 2 and 3 km/s, starting from the hypocenter.

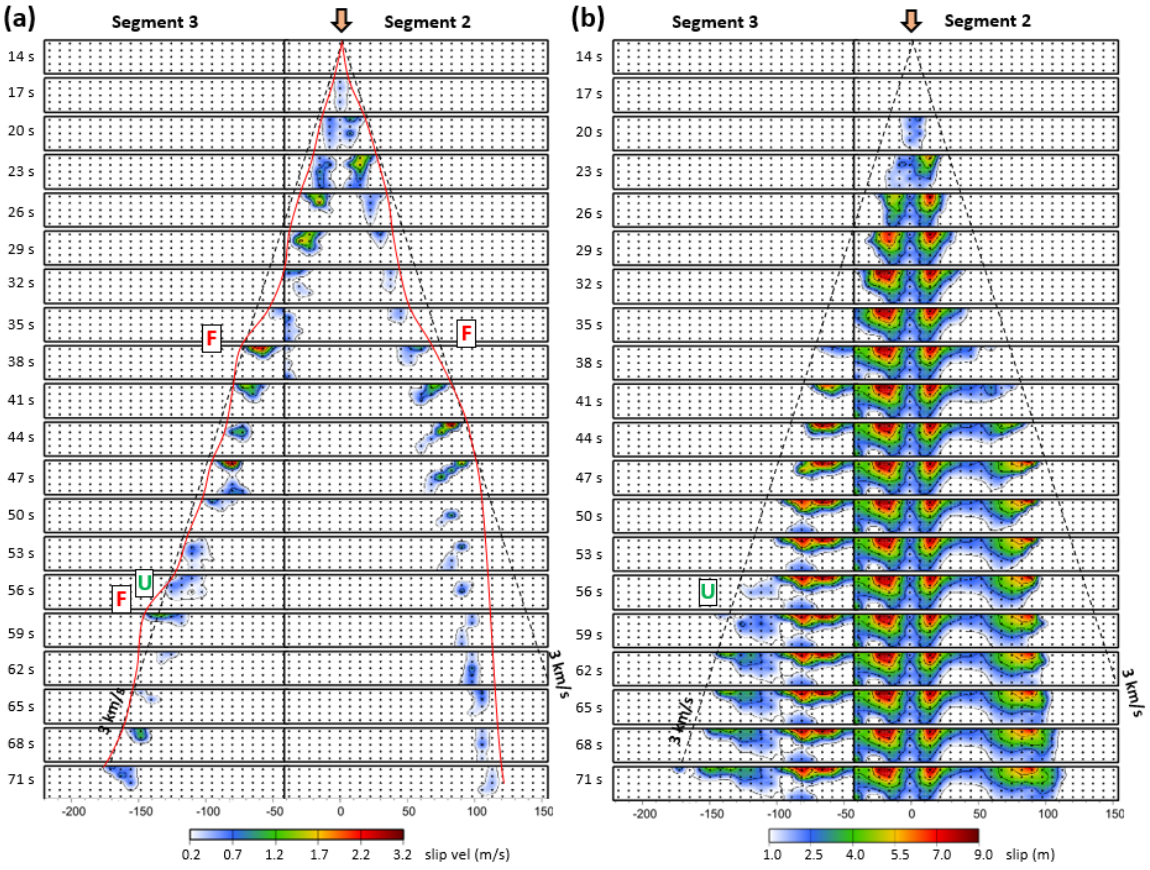

Figure 7. Snapshots of the space-time evolution of the rupture on segments 3 and 4 (EAF) from the joint inversion of strong motion and GNSS data. **(a)** slip velocity at each time step, **(b)** cumulative slip. Time steps are indicated on the left side. Oblique dashed black lines: reference slope corresponding to average rupture velocity (Vr) 3 km/s, starting from the junction with the splay fault (orange arrow). The red curve in **(a)** tracks the rupture front with its variations. Boxes labeled F (fast) in red point to areas of increased local Vr, reaching supershear, related to the F markers in **Figure 5c.** Box labeled U (underneath) in green indicates where the slip is moving below the near-surface area that will slip about 4 m in the following seconds.

The overall source time function is shown in **Figure 8a**, together with those corresponding to the NE-ward part of the rupture **(Figure 8b)** and to the SW-ward part of the rupture **(Figure 8c)**. The total duration of the rupture is about 80 s, with the NE and SW parts contributing simultaneously between 15 to 72s. The initial pulse on **Figure 8a** (0 – 15 s) is due solely to the splay fault. The overall moment magnitude Mw is 7.83. The moment magnitudes of the NE part, the SW part, and the splay fault are 7.58, 7.64, and 6.98, respectively.

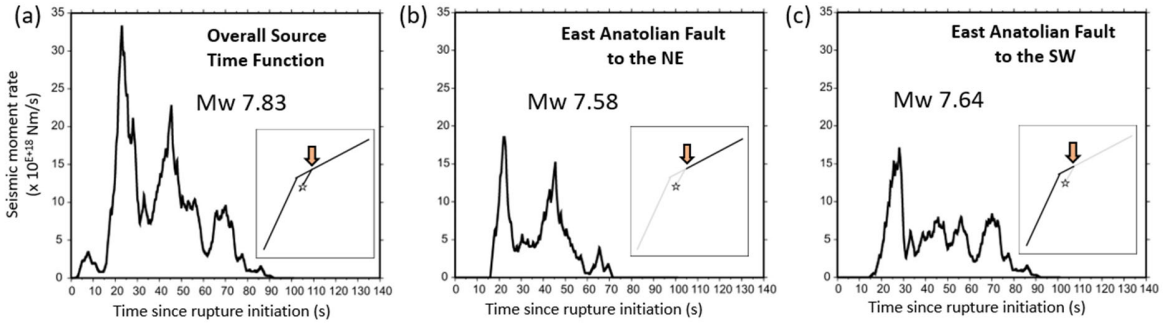

Figure 8. (a) Overall source time function (all rupture segments). **(b**) Source time function for the part of the East Anatolian Fault rupturing to the North-East from the junction with the splay fault. **(c)** Source time function for the part of the East Anatolian Fault rupturing to the South-West from the junction with the splay fault. The corresponding moment magnitude Mw is indicated in each case, and the rupture segments involved are shown with heavy black lines in the inner frame. Orange arrow: junction. Open star: epicenter. From the joint inversion of strong motion and GNSS data.

392 The data fitting of the strong motion records integrated to displacement is shown on **Figure 9**,

393 and that of the horizontal GNSS offsets on **Figure 10**.

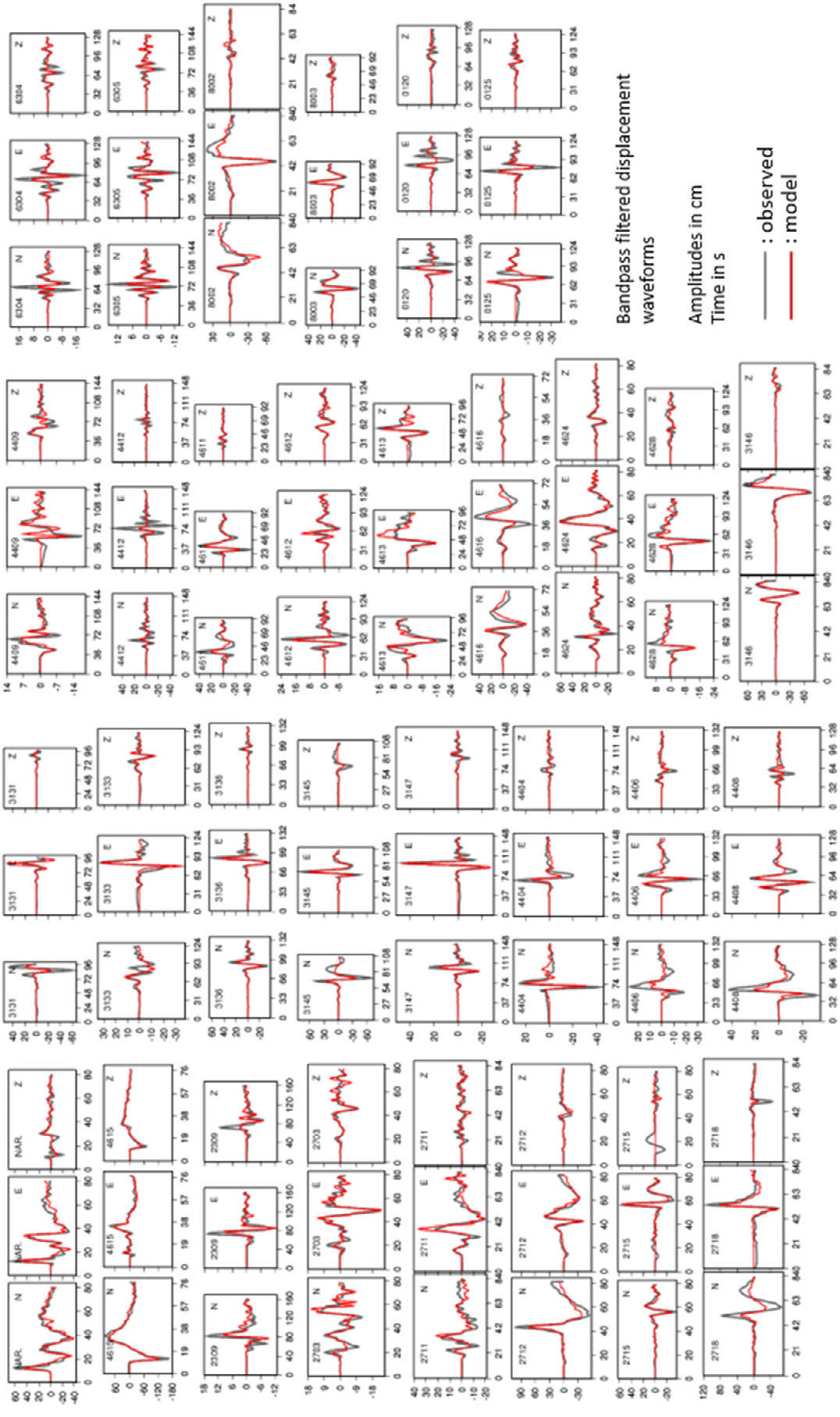
Bandpass filtered displacement
waveforms
Amplitudes in cm
Time in s
: observed
: model

Figure 9. Waveform fitting by joint inversion of strong motion and GNSS data. N, E, Z: north, east, vertical (up) components respectively. All displacement waveforms bandpass filtered.

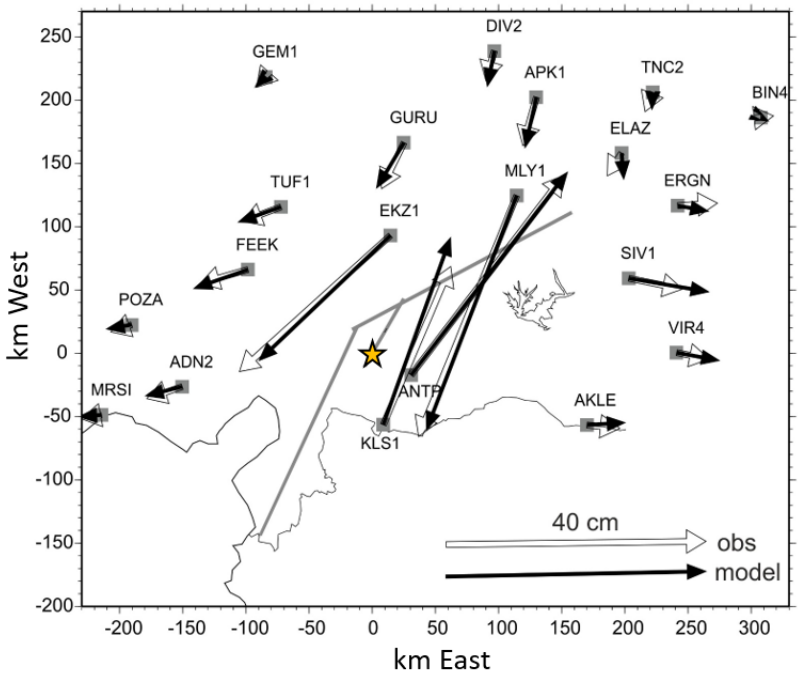

Figure 10. Horizontal GNSS offsets fitting by joint inversion of strong motion and GNSS data. Orange star: epicenter. Heavy gray lines: trace of fault model. Obs: observed.

Discussion

Rupture velocity along the splay fault

406 Rosakis et al. (2023) analyzed the records of strong motion stations NAR and 4615, integrated to
407 velocity and rotated to fault parallel (FP) and fault normal (FN) components with respect to the
408 splay fault assuming a strike of N22°. According to their analysis, based on theoretical and
409 laboratory experiments, the observed ratio FP/FN of 1.2 at station NAR is the signature of a
410 supershear rupture (FP/FN > 1). They further found that station 4615 is located at the transition
411 from sub-shear to supershear rupture.

412 Here, we find that ground displacement waveforms in the frequency band 0.01 to 0.3 Hz at
413 stations 4615 and NAR can be modeled correctly with a constant sub-shear rupture velocity on
414 the splay fault, as low as 2.5 km/s (**Figure 2a**). The question then arises whether the supershear
415 signature is present only on velocity signals, possibly only on unfiltered ones. In a first step, we
416 verified that the FP component of NAR is effectively larger than its FN component in velocity, both
417 on the unfiltered and on the 0.01 to 1 Hz bandpass filtered signals (**Figure S5** in the electronic
418 supplement to this article). This is illustrated for two possible azimuths of the splay fault, N22°
419 and N30°. In a second step, we verified that it is possible to model the velocity signals of both
420 stations NAR and 4615 without a transition to supershear (**Figure S6** in the electronic supplement
421 to this article). The modeling is done in the frequency band 0.01 to 1 Hz by finely discretizing the
422 rupture segment corresponding to the splay fault, but limiting its spatial dimensions to the
423 minimum necessary to model the first 15 s of signal, which include the main pulse associated with
424 the suspected supershear Mach front identified by Rosakis et al. (2023). The amplitude of the
425 main velocity pulse is correctly matched using a constant rupture velocity of 2.8 km/s all along
426 the splay fault, both on the N and E components and on the FP and FN components (**Figure S6** in
427 the electronic supplement to this article).

The rupture speed on the splay fault can be influenced by the distance (L) separating the initiation of the rupture from stations NAR and 4615, approximately 22 km in our main inversion (**Figure 2**). In order to evaluate this potential uncertainty, we carried out two additional inversions, one by shifting the hypocenter by 7.5 km towards the SSW, corresponding to an increase of L (29.5 km), the other by shifting it by the same value towards the NNE, corresponding to a smaller L (14.5 km). To explore whether a supershear rupture is required, we increased the value of Vrmax (bounding velocity) to 4 km/s. The delay used for the minimum onset time of rupture on the EAF is also adapted, to 16 s for the longer L and to 12 s for the shorter L, instead of 14 s in our intermediate main inversion.

The result is shown in **Figure S7** of the electronic supplement to this article. For the longer L (**Figure S7a**), rupture speed on the splay fault reaches 3.5 km/s, while for the shorter L (**Figure S7c**), rupture speed is overall below 2.8 km/s, showing a trade-off between distance L and rupture speed. All three positions of the epicenter provide similar quality of data fit, meaning that the position of the epicenter is not well constrained, and that the rupture velocity on the splay fault may be considered as 3.0 +/- 0.5 km/s. Perhaps in the extreme case where the rupture speed reaches 3.5 km/s on the splay fault, we are at the limit of supershear, especially at shallow depth near the two stations 4615 and NAR. If the rupture speed is supershear relative only to the shallow seismic speeds, maybe that could be sufficient to make FP/FN>1 and that would reconcile our results with those of Rosakis et al. (2023). In any case, the rupture speed remains well below the supershear peaks observed along the EAF and which reach 4 km/s and higher (**Figure 5**).

449 We nevertheless conclude that the criterion FP/FN > 1 is not necessarily the signature of a
450 supershear rupture, and that the main pulse observed in the initial part of the records of stations
451 NAR and 4615 can be explained by left-lateral shallow faulting propagating at sub-shear velocity
452 between the two stations.

453 The failure of the FP/FN criterion could be caused by a level of complexity of the rupture that has
454 not been accounted for in the underlying theoretical models and laboratory experiments. Indeed,
455 on the SPF the slip emerges at the surface at a substantial distance NE of the epicenter. This
456 pattern is reminiscent of the Mw 6.0 2014 South Napa, California earthquake, in which the
457 rupture propagated within a narrow corridor upward and obliquely from the hypocenter (Premus
458 et al., 2022). In contrast, the FP/FN criterion to distinguish sub-shear and supershear ruptures
459 arises from theoretical and experimental models with relatively more simple rupture front
460 geometries (Aagaard and Heaton, 2004; Dunham and Arhuleta, 2004; Bizzarri et al., 2010; Mello
461 et al., 2016).

462 *Resolution of the kinematic model*

463 We carried out a synthetic test to assess the resolution of the kinematic inversion. We designed
464 a synthetic kinematic model with variable slip and variable rupture velocity as shown in **Figure**
465 **S8-left** (slip distribution) and **Figure S9** (gray dots, rupture timing) in the electronic supplement
466 to this article. Based on this model, we generated synthetic displacement waveforms and static
467 offsets at the same strong motion and GNSS stations as for the real data. Amplitudes of the
468 synthetic data were randomly modified by a factor 1.1 or 0.9 at each station (10% change). These
469 modified synthetic data were inverted using exactly the same rupture parameterization and

algorithm than our real data inversion. However, we used a slightly modified 1D velocity model to compute the Green's function (model of **Table S1** to generate the synthetic data, model of **Table S2** for the inversion, both in the electronic supplement to this article), to avoid unrealistically perfect conditions. Overall, the main features of the synthetic model are retrieved. Nevertheless, there is some spreading of slip zones and poorer timing resolution of moderate amplitude slip patches on the NE propagating portion of the rupture, which can be related to the smaller number of stations and their relatively greater distance from the rupture on this part of the source. We also observe an overestimation of the subfault onset time at the NE termination of the splay fault. It can be assumed that the same effects occur with the real data.

Near source stations and discretization

Along segment 3 of the model (the southwesternmost branch of the EAF), the point sources are spaced 7.5 km along strike and 5 km along dip (**Table 1**), while the distance from the model fault to the nearest stations 3131 and 2712 is 1.5 to 2 km. On segment 1bis (splay fault), the point source spacing is 0.5 km along strike and 1 km along dip, while stations NAR and 4615 are located about 0.8 km from the fault model. This raises the question of whether the discretization used for these segments is fine enough, since the point source approximation requires a source dimension, i.e. a point source spacing, smaller than the distance to the stations. A second question is to what extent the data fit and rupture properties of the model depend on the positioning of the point sources, especially for segment 3 whose lateral spacing, 7.5 km, is quite large compared to the distance to the nearest stations. To assess this, we performed two specific tests.

In the first test, we adopted an alternative approach introduced in Delouis et al. (2002), which superimposes a finer grid of second order point sources on each subfault. To limit the number of invertible parameters, slip and rupture speed remain constant on each individual subfault. This allows for a better representation of source finiteness continuity without multiplying the number of unknown parameters to be inverted for. This is done for segments 3 and 1bis only, with a second order point source spacing of 0.8 km and 0.1 km respectively. This spacing is used both along strike and dip. For each subfault, rupture propagation starts at an initiation point which is no longer the center of the subfault but which is the second order point source closest to the hypocenter for segment 1bis, and closest to the junction between segment 2 and 3 (bend of the EAF) for segment 3. This initiation point is located at the frontier of the subfault, systematically at its northeastern side in the present case. For the propagation of the rupture locally on the sub-fault, we use a rupture speed of 3 km/s which is approximately the average rupture speed found for those segments. It should be noted that the imposition of a constant rupture velocity and slip is only valid locally at the scale of the individual subfaults, i.e. to fix the initiation times and the slip of the second-order source points, save the initiation point. The triggering time of the subfaults (i.e. the onset time of its initial second order point source on its northeastern side) and their slip value are inverted as before, which still allows the rupture to show overall variations in slip and rupture speed. Segment 1 and 2 are left as before, with a single point source at the center of their subfaults.

The second test is an inversion with the same resolution of discretization as our initial inversion, but with the node points on segment 3 shifted along its strike, so that new point source centers

512 are located in between their initial positions. In other words, points sources have been shifted
513 by 3.75 km along strike.

514 Both test inversions showed little variation in the resulting kinematic rupture models and a data
515 fit similar to that of our main inversion detailed in this article (**Figures S10 to S13** of the electronic
516 supplement to this article). However, it can be noted that the near-surface slip in the southern
517 part of slip zone a3 shows more significant variations, reflecting a certain dependence on the
518 discretization (**Figure S10**). Similarly, we observe that the peak rupture speed on the portion of
519 the EAF between 100 and 150 km southwest of the junction varies between 4 km/s and 4.5 km/s
520 from one inversion to another, indicating a locally larger uncertainty, although we remain in the
521 supershear domain (**Figure S12**)

522 *Rupture transition from the splay fault to the East Anatolian Fault*

523 In our final model, rupture starts on the EAF at 14 s after the earthquake onset, before the
524 development of slip at the termination of the splay fault between 17 and 24 s (**Figure 4a and 6a**).
525 This suggests that rupture on the EAF was triggered before the end of rupture on the splay fault.
526 However, we have shown that a constant rupture speed of 3 km/s, or even a little faster, on the
527 splay fault produces an equally low RMS misfit of the data (**Figure 2**). At 3 km/s, the rupture arrives
528 at the junction with the EAF approximately 14 s after origin time, leading to a continuous rupture
529 from the splay fault to the EAF. We acknowledge an uncertainty of a few seconds on the timing
530 of the end of the rupture of the splay fault, as observed in the synthetic test. This uncertainty
531 could possibly be linked to a trade-off with the slip on the EAF at the junction, which in turn may
532 be due to the absence of strong motion stations very close to the junction.

The uncertainty in resolving the slip at the termination of segment 1 is confirmed by an additional test inversion in which rupture onset time on segment 1 is not permitted to exceed 14 s. This leads to an almost complete disappearance of the slip at the end of the segment, without degradation of the data fit nor modification of the other properties of the final kinematic model. We conclude that in the time span 14 to 17 s after rupture initiation there are few constraints on the kinematics of the rupture, which may have become evanescent on the splay fault a few km after passing between stations NAR and 4615, heading NNE towards the junction with the EAF.

Necessity of local rupture speed variations

To further evaluate whether rupture velocity variations along the EAF are indeed required by the data, we performed an additional test in which a constant velocity of 3 km/s is imposed on segments 2 and 3. The negative impact of this constant velocity assumption on waveform modeling is clear at stations near the SW-ward rupture along segment 3 (**Figure S14** in the electronic supplement to this article). The effect is less clear at stations around the NE-ward rupture along segment 2. We conclude that variations in Vr are well-constrained by the data, especially for the SW branch of the rupture, which is the best resolved part of the source owing to the presence of several stations in close proximity.

Comparison with other kinematic models

Two kinematic models obtained by inversions of multiple data, including strong motion records, have been published previously. These are the USGS finite fault model and that of Melgar et al. (2023). The data used are not the same, although they partially overlap with each other and with ours. While our study relies primarily on the dense network of strong motion instruments, the

554 two previous studies use a smaller subset of strong motion records and combine other data types
555 such as HR-cGNSS time series (which are not very close to the rupture), teleseismic data and InSAR
556 data. Note that Melgar et al. (2023) model both the Mw 7.8 and 7.6 earthquakes that occurred
557 on the same day in SE Turkey, which are covered by the same InSAR data.

558 Our kinematic model has in common several major features with the above mentioned models:
559 the initiation on the splay fault with moderate slip, followed by bilateral propagation on the EAF,
560 a more superficial rupture on the south-westernmost segment of the rupture, a maximum slip of
561 the order of 8 to 9 m on the EAF. We confirm that the average rupture velocity along the EAF did
562 not exceed about 3.2 km/s, as stated by Melgar et al. (2023). However, by modeling more strong
563 motion records, particularly the NAR and 4615 stations near the splay fault that were not
564 incorporated in previous studies, as well as other stations along the EAF, we find remarkable
565 features of rupture propagation that have not been fully addressed before, in particular the
566 existence of several portions where the rupture front propagates at supershear speeds along the
567 EAF.

568 The fact that a little more seismic moment release is observed SW of the junction (Mw 7.64) than
569 NE (Mw 7.58) is contrary to what the models derived from geodetic data (SAR) show (e.g. Melgar
570 et al., 2023; Barbot et al., 2023). This difference may be due to a bias linked to the lower density
571 of the strong motion network along the NE branch of the EAF. However, Mai et al. (2023) similarly
572 found larger slip values along the SW branch in their model derived from the inversion of
573 teleseismic data than in their geodetic model. We speculate that the difference between geodetic
574 (SAR) and seismological models may be related to the lower sensitivity of SAR data for the SW

branch (segment 3 of our model), which is oriented more perpendicular to the satellite line of sight than the NE branch (segment 2 of our model).

Transient supershear speeds

The spatial fluctuations of local rupture speed are among the earthquake source properties that are most difficult to constrain robustly, often due to scarcity of near-fault seismological data. Transient supershear rupture was recently reported for the 2021 Mw 7.3 Madoi, China earthquake using teleseismic back-projection analysis (Cheng et al., 2023), a technique that was essential to reveal the steady supershear propagation of the 2018 Mw 7.5 Palu, Indonesia earthquake (Bao et al., 2019). While systematic studies of global earthquakes show that teleseismic back-projection can constrain well their average rupture speeds (Bao et al., 2022), spatial fluctuations of rupture speed at scales of 10 km or less are best resolved with local strong motion observations, as done in our present study.

Our source inversion results regarding rupture speed challenge simple models of dynamic rupture. Theoretical models of steady ruptures with large aspect ratio (rupture length much larger than rupture width), including supershear ruptures (Weng and Ampuero, 2020), predict a correlation between final slip and rupture speed. We do not find such a correlation in our inversion results (**Figure 5**). This implies that the exceptional dataset available for the 2023 Mw 7.8 Turkey earthquake warrants further extensions of current theories, which so far assume simple rupture fronts or depth-averaged rupture properties (Weng and Ampuero, 2019). The intermittent supershear bursts found here might result from 3D rupture patterns that cannot be

596 captured by 2.5D models. A possible scenario, proposed in dynamic rupture models by Dunham
597 et al (2003) and Page et al (2005), is a rupture front that reaches the edge of an asperity, goes
598 around it, then breaks it and generates a burst of rupture acceleration to supershear. The fine-
599 scale details of such a pattern may not be resolvable by kinematic source inversion, even though
600 its coarser effect on rupture speed is, and may warrant elucidation by dynamic source inversions
601 (e.g. Premus et al, 2022).

602

603 **Conclusions**

604 Taking advantage of the exceptional strong motion dataset made available by the Turkish Disaster
605 and Emergency Management Authority (AFAD), which had been used less comprehensively by
606 previous studies, and to a lesser extent of GNSS static data, we determine the rupture
607 characteristics of the February 6, 2023 Mw 7.8 earthquake in southeast Turkey.

608 We explore in detail the rupture properties required to model the seismograms recorded by two
609 stations, NAR and 4615, located very close to the splay fault on which the earthquake started. We
610 show that supershear rupture speed is not required on the splay fault. Indeed, these seismograms
611 can be correctly modeled, in displacement and in velocity, by a sub-shear rupture passing
612 between the two stations with about 4 m of slip at or near the surface.

613 About 14 s after rupture initiation, the rupture on the splay fault reached the East Anatolian Fault
614 (EAF). It then propagated bilaterally along the EAF, extending about 120 km NE and 180 km SW.
615 The depth extent of the rupture decreases as it passes the bend of the EAF to the SW. The highest

slip values are located near the surface on each rupture segment, with a maximum of 8 m +/- 2 m along the EAF.

The along-strike averaged rupture velocity remains below about 3.3 km/s, but locally, when entering strong slip zones after crossing weak slip zones, the rupture velocity becomes supershear for a few tens of kilometers. This pattern of rupture deceleration and acceleration is observed at three different locations along the EAF, thanks to the exceptionally dense near-fault recordings available.

Lateral progression of the rupture generally begins at or near the surface before propagating at depth, with a notable exception in the south-westernmost part of the rupture where a slip patch at the surface breaks after the rupture has surrounded it at larger depth.

Acknowledgments

B.D. and J.P.A. are partially funded by the EU project “A Digital Twin for Geophysical Extremes” (DT-GEO, No. 101058129). J.P.A. is also funded by the French government through the UCA-JEDI Investments in the Future project (ANR-15-IDEX-01) managed by the National Research Agency (ANR). M.vdE is supported by the European Research Council (ERC) under the European Union’s Horizon 2020 research and innovation programme (grant agreement No. 101041092 - ABYSS). We are most grateful to the three reviewers, two anonymous and A. Ozgun Konca, who helped us in improving the manuscript.

Data and resources

Electronic Supplement 1 contains figures (S1 to S9) and two additional Tables (S1 and S2) cited in the manuscript, which provide additional support for our results. Electronic Supplement 2 contains the finite fault model in text format.

The strong motion data were retrieved from the Disaster and Emergency Management Authority of Turkey (AFAD) - Disaster and Emergency Management Authority. (1973). Turkish National Strong Motion Network [Data set]. Department of Earthquake, Disaster and Emergency Management Authority https://doi.org/10.7914/SN/TK) using https://tadas.afad.gov.tr/login https://tadas.afad.gov.tr/list-event (last accessed on February 16, 2023).

GPS data were retrieved from the Nevada Geodetic Laboratory (Blewitt et al., 2018) using http://geodesy.unr.edu/ (last accessed on 9 March 2023).

USGS Turkey Earthquake Emergency Response (Reitmann et al., 2023). (https://usgs.maps.arcgis.com/apps/webappviewer/index.html?id=5229bb842bd64b688d769abbefe43b46), last accessed on 9 March 2023.

Kahramanmaraş Supersite science web (http://geo-gsnl.org/kahramanmaras-supersite-science-page/) (last accessed on March 9, 2023).

Some figures were partly made using the Generic Mapping Tools (GMT) package by Wessel et al. (2019) (https://www.generic-mapping-tools.org/) (last accessed on April 17, 2023).

Seismic data processing was partly done using the Seismic Analysis Code (SAC) package by Goldstein et al. (2003) and Goldstein and Snoke (2005)

(http://ds.iris.edu/ds/nodes/dmc/software/downloads/sac/102-0/ (last accessed on April 12, 2023).

References

Aagaard, B. T., and T. H. Heaton (2004). Near-source ground motions from simulations of sustained intersonic and supersonic fault ruptures. *Bull. Seismol. Soc. Am.*, 94 (6), 2064-2078.

Bao, H., Ampuero, J. P., Meng, L., Fielding, E. J., Liang, C., Milliner, C. W., Feng, T., & Huang, H. (2019). Early and persistent supershear rupture of the 2018 magnitude 7.5 Palu earthquake. *Nature Geoscience*, 12(3), 200-205.

Bao, H., Xu, L., Meng, L., Ampuero, J. P., Gao, L., & Zhang, H. (2022). Global frequency of oceanic and continental supershear earthquakes. *Nature Geoscience*, 15, 942–949.

Barbot S., H. Luo, T. Wang, Y. Hamiel, O. Piatibratova, T. Muhammad, C. Braitenberg, and G. Gurbuz(2023). Slip distribution of the February 6, 2023 Mw 7.8 and Mw 7.6, Kahramanmaraş, Turkey earthquake sequence in the East Anatolian Fault Zone. *Seismica*. 2023;3(2). https://doi.org/10.26443/seismica.v2i3.502

Bizzarri, A., Dunham, E. M., & Spudich, P. (2010). Coherence of Mach fronts during heterogeneous supershear earthquake rupture propagation: Simulations and comparison with observations. *Journal of Geophysical Research: Solid Earth*, 115 (B8), B08301.

Blewitt, G., W. C. Hammond, and C. Kreemer (2018), Harnessing the GPS data explosion for interdisciplinary science, *Eos, 99,* https://doi.org/10.1029/2018EO104623.

676 Bouchon, M. (1981). A simple method to calculate Green's functions for elastic layered media,
677 *Bull. Seismol. Soc. Am.*, 71 (4), 959–971.

678 Cheng, C., D. Wang, Q. Yao, L. Fang, S. Xu, Z. Huang, T. Liu, Z. Wang and X. Huang (2023). The
679 2021 Mw 7.3 Madoi, China Earthquake: Transient Supershear Ruptures on a Presumed Immature
680 Strike-Slip Fault. *Journal of Geophysical Research: Solid Earth*, 128 (2), e2022JB024641.

681 Delouis, B., D. Giardini, P. Lundgren, and J. Salichon (2002). Joint inversion of InSAR, GPS,
682 teleseismic and strong motion data for the spatial and temporal distribution of earthquake slip:
683 Application to the 1999 Izmit Mainshock, *Bull. Seism. Soc. Am.*, 92, 278-299.
684 https://doi.org/10.1785/0120000806

685 Delouis, B., E. Oral, M. Menager, J.-P. Ampuero, A. Guilhem Trilla, M. Régnier, and A. Deschamps
686 (2021). Constraining the point source parameters of the 11 November 2019 Mw 4.9 Le Teil
687 earthquake using multiple relocation approaches, first motion and full waveform inversions,
688 *Comptes Rendus Géoscience* 353(S1):1-24. DOI : https://doi.org/10.5802/crgeos.78

689 Dunham, E. M., Favreau, P., & Carlson, J. M. (2003). A supershear transition mechanism for cracks.
690 *Science*, 299 (5612), 1557-1559.

691 Dunham, E. M., and R. J. Archuleta (2004). Evidence for a supershear transient during the 2002
692 Denali fault earthquake, *Bull. Seismol. Soc. Am.*, 94 (6B), S256-S268.

693 Goldstein, P., D. Dodge, M. Firpo, and L. Minner (2003). "SAC2000: Signal processing and analysis
694 tools for seismologists and engineers, Invited contribution to "The IASPEI International Handbook
695 of Earthquake and Engineering Seismology", Edited by WHK Lee, H. Kanamori, P.C. Jennings, and
696 C. Kisslinger, Academic Press, London.

697 Goldstein, P., and A. Snoke, (2005). “SAC Availability for the IRIS Community”, *Incorporated*
698 *Institutions for Seismology* Data Management Center Electronic Newsletter.

699 Güvercin, S. E., H. Karabulut, A. Ö. Konca, U. Doğan, and S. Ergintav (2022). Active seismotectonics
700 of the East Anatolian Fault, *Geophysical Journal International*, Volume 230, Issue 1, Pages 50–69,
701 https://doi.org/10.1093/gji/ggac045

702 Johnson, L. (1974). Green's function for Lamb's problem, *Geophys. J. R. Astr. Soc*. 37, 99-131.

703 Karabacak, V., Ç. Özkaymak, H. Sözbilir, O. Tatar, B. Aktuğ, Ö. Cevdet Özdağ, R. Çakir, E. Aksoy, F.
704 Koçbulut, M. Softa, E. Akgün, A. Demir, and G. Arslan (2023). The 2023 Pazarcık (Kahramanmaraş,
705 Türkiye) earthquake (Mw 7.7): implications for surface rupture dynamics along the East Anatolian
706 Fault Zone. *Journal of the Geological Society*, 180 (3): jgs2023–020. doi:
707 https://doi.org/10.1144/jgs2023-020

708 Karabulut, H., S. E. Güvercin, J. Hollingsworth, and A. Ö. Konca (2023). Long silence on the East
709 Anatolian Fault Zone (Southern Turkey) ends with devastating double earthquakes (6 February
710 2023) over a seismic gap: implications for the seismic potential in the Eastern Mediterranean
711 region. *Journal of the Geological Society,* 180 (3): jgs2023–021. doi:
712 https://doi.org/10.1144/jgs2023-021

713 Legrand, D. (1995). Etude conjointe de la source d'une population de séismes tectoniques ou
714 volcaniques en champ proche : de la sismologie classique aux effets non linéaires, Ph.D. Thesis,
715 Université Louis Pasteur, Strasbourg (FR), 204 pp.

716 Mai, P. M., T. Aspiotis, T. A. Aquib, E. V. Cano, D. Castro-Cruz, A. Espindola-Carmona, B. Li, X. Li, J.
717 Liu, R. Matrau, A. Nobile, K. H. Palgunadi, M. Ribot, L. Parisi, C. Suhendi, Y. Tang, B. Yalcin, U. Avşar,

718 Y. Klinger, and S. Jónsson (2023). The Destructive Earthquake Doublet of 6 February 2023 in
719 South-Central Türkiye and Northwestern Syria: Initial Observations and Analyses. *The Seismic*
720 *Record*, 3 (2): 105–115. doi: https://doi.org/10.1785/0320230007

721 Mello, M., H. S. Bhat, and A. J. Rosakis (2016). Spatiotemporal properties of Sub-Rayleigh and
722 supershear rupture velocity fields: Theory and experiments. *Journal of the Mechanics and Physics*
723 *of Solids*, 93, 153-181.

724 Meng L., H. Bao, H. Huang, A. Zhang, A. Bloore, and Z. Liu (2018). "Double Pincer Movement:
725 Encircling Rupture Splitting During the 2015 Mw 8.3 Illapel Earthquake", *Earth and Planetary*
726 *Science Letters*, 495, pp. 164-173. https://doi.org/10.1016/j.epsl.2018.04.057

727 Page, M. T., E.M. Dunham, and J. M. Carlson, (2005). Distinguishing barriers and asperities in near-
728 source ground motion. *Journal of Geophysical Research: Solid Earth*, 110 (B11), B11302.

729 Premus, J., F. Gallovič, and J.-P. Ampuero (2022). Bridging time scales of faulting: From coseismic
730 to postseismic slip of the M w 6.0 2014 South Napa, California earthquake. *Science Advances*, 8
731 (38), eabq2536.

732 Reitman, N. G, R. W. Briggs, W. D. Barnhart, J. A. Thompson Jobe, C. B. DuRoss, A. E. Hatem, R. D.
733 Gold, J. D. Mejstrik, and S. Akçiz (2023) Preliminary fault rupture mapping of the 2023 M7.8 and
734 M7.5 Türkiye Earthquakes. DOI: https://doi.org/10.5066/P985I7U2

735 Rosakis, A., M. Abdelmeguid, and A. Elbanna (2023). Evidence of Early Supershear Transition in
736 the Mw 7.8 Kahramanmara\c {s} Earthquake From Near-Field Records. *arXiv preprint*
737 arXiv:2302.07214. https://arxiv.org/ftp/arxiv/papers/2302/2302.07214.pdf

738 Savage, J. C. (1980). Dislocations in seismology, in Dislocations in solids, F. R. N. Navarro (Editor),
739 North-Holland, Amsterdam

740 USGS finite source model (2023).
741 https://earthquake.usgs.gov/earthquakes/eventpage/us6000jllz/finite-fault

742 Weng, H., & Ampuero, J. P. (2019). The dynamics of elongated earthquake ruptures. *Journal of*
743 *Geophysical Research: Solid Earth*, 124 (8), 8584-8610.

744 Weng, H., & Ampuero, J. P. (2020). Continuum of earthquake rupture speeds enabled by oblique
745 slip. *Nature Geoscience*, 13 (12), 817-821.

746 Wessel, P., J. F. Luis, L. Uieda, R. Scharroo, F. Wobbe, W. H. F. Smith, and D. Tian (2019). The
747 Generic Mapping Tools version 6. Geochemistry, Geophysics, *Geosystems*, 20, 5556–5564.
748 https://doi.org/10.1029/2019GC008515

749 Zhang, G., M. Vallée, X. Shan, and B. Delouis (2012). Evidence of sudden rupture of a large
750 asperity during the 2008 Mw7.9 Wenchuan earthquake based on strong motion analysis.
751 *Geophysical Research Letter*, L17303, doi:10.1029/2012GL052516.

752 **List of Figure captions**

753 **Figure 1.** (a) Overview map showing the strong motion (green diamond) and GNSS (red squares)
754 stations used in this study, with corresponding names. Thick black line: surface trace of the fault
755 model. Orange star: epicenter of the mainshock (37.22°N, 37.025°E, this study) at the origin of
756 the coordinates (0,0). The dashed box indicates the zone (b). (b) Close-up of the epicentral area.
757 Thin lines with small dots show the fault model with the position of the point sources (simplified

758 representation, each dot corresponding in reality to 5 points distributed along dip), projected on
759 the earth surface. The names of the fault segments are shown. The dashed frame indicates the
760 zone (c). Orange arrow: junction between segment 1-1bis (splay fault) and segment 2 (East
761 Anatolian Fault). (c) Close-up of the area where the fault model passes between the strong motion
762 stations 4615 and NAR and where a finely discretized fault segment 1bis is used. SPF: splay fault;
763 EAF: East Anatolian Fault.

764

765 **Figure 2.** Exploration of the rupture velocity (Vr) on segments 1 and 1bis. (a) RMS waveform misfit
766 value for all strong motion stations (SM) and for 4615 and NAR only as a function of fixed constant
767 Vr values. (b) North component waveform fit for NAR and 4615 stations for constant Vr values of
768 2.0, 2.8 and 5.0 km/s. Waveforms are in displacement and bandpass filtered between 0.01 and
769 0.3 Hz. Only the north components of NAR and 4615, being the most sensitive to Vr and the most
770 difficult to model, are shown but the inversion is performed with the three components N, E and
771 Z of all strong motion stations.

772

773 **Figure 3.** Slip distribution from the joint inversion of strong motion and GNSS data on the three
774 segments of the kinematic model, and relation with the map view. SPF: splay fault; EAF East
775 Anatolian Fault. On the map, the epicenter, the surface trace of the rupture model, and the strong
776 motion stations are represented by the orange star, the red lines and the green diamonds
777 respectively. The hypocenter on segment 1-1bis (SPF) is marked by the open triangle. The junction
778 between the splay fault (SPF, segment 1) and Segment 2 of the EAF is marked by the orange

arrow. a1 to a5: labels for the main slip areas along the EAF. The slip direction is indicated by the open arrows scaled with slip amplitude.

Figure 4. Time-distance plots of slip for segments 1 and 1bis (a) and for segments 2 and 3 (b) from the joint inversion of strong motion and GNSS data. SPF: splay fault; EAF: East Anatolian Fault; orange dots: subfault timing at a function of distance, with size proportional to slip (larger than 1 m). Green shaded area: allowed domain for average rupture speed. Oblique black line: average rupture speed 3 km/s. Lines of average rupture speed start from the hypocenter in (a) and from the junction between the splay fault (segment 1) and the EAF (segment 2) in (b). The slip distribution along strike and dip is shown above the graphs. On top of (a), the position along strike of strong motion stations 4615 and NAR is indicated, and on top of (b), the junction with the splay fault is indicated by the orange arrow. a1 to a5: labels for the main slip areas along the EAF.

Figure 5. Estimation of rupture speed as a function of distance from the junction along the EAF (Segment 2 and 3). (a) Inverted rupture acceleration. (b) Local rupture speed (integral of acceleration). (c) Black curve: rupture onset time (related to the second integral of acceleration). The markers represent the observed onset times colored according to the estimated local rupture speed. Compared to Fig. 4b, only the subfaults whose time is less than 1 s from the rupture front at a given horizontal position are included in the inversion and panel c. The shaded regions indicate the locations of low slip. F (fast) markers in red point to areas of high local speed, reaching supershear. Slip map on top with the same labels as in previous Figures.

800

801 **Figure 6.** Snapshots of the space-time evolution of the rupture on segments 1 and 1bis (splay
802 fault) from the joint inversion of strong motion and GNSS data. (a) slip velocity at each time step,
803 (b) cumulative slip. Time steps are indicated on the left side. Open triangle: hypocenter. Oblique
804 dashed black lines: reference slopes corresponding to average rupture velocities (Vr) 2 and 3
805 km/s, starting from the hypocenter.

806

807 **Figure 7.** Snapshots of the space-time evolution of the rupture on segments 3 and 4 (EAF) from
808 the joint inversion of strong motion and GNSS data. (a) slip velocity at each time step, (b)
809 cumulative slip. Time steps are indicated on the left side. Oblique dashed black lines: reference
810 slope corresponding to average rupture velocity (Vr) 3 km/s, starting from the junction with the
811 splay fault (orange arrow). The red curve in (a) tracks the rupture front with its variations. Boxes
812 labeled F (fast) in red point to areas of increased local Vr, reaching supershear, related to the F
813 markers in Figure 5c. Box labeled U (underneath) in green indicates where the slip is moving below
814 the near-surface area that will slip about 4 m in the following seconds.

815

816 **Figure 8.** (a) Overall source time function (all rupture segments). (b) Source time function for the
817 part of the East Anatolian Fault rupturing to the North-East from the junction with the splay fault.
818 (c) Source time function for the part of the East Anatolian Fault rupturing to the South-West from
819 the junction with the splay fault. The corresponding moment magnitude Mw is indicated in each
820 case, and the rupture segments involved are shown with heavy black lines in the inner frame.

Orange arrow: junction. Open star: epicenter. From the joint inversion of strong motion and GNSS data.

Figure 9. Waveform fitting by joint inversion of strong motion and GNSS data. N, E, Z: north, east, vertical (up) components respectively. All displacement waveforms bandpass filtered.

Figure 10. Horizontal GNSS offsets fitting by joint inversion of strong motion and GNSS data. Orange star: epicenter. Heavy gray lines: trace of fault model. Obs: observed.

Mailing address of Authors:

B.D., M.vdE, and J-P.A.: CNRS-GEOAZUR, Campus Azur, 250 rue Albert Einstein, CS 10269,

06905 Sophia Antipolis Cedex, France

Email address: delouis@geoazur.unice.fr, Martijn.VANDENENDE@oca.eu,

ampuero@geoazur.unice.fr